Approximate Factorization Algorithm for Three-Dimensional Transonic Nacelle/Inlet Flowfield Computations

Joseph Vadyak* and Essam H. Atta*
Lockheed-Georgia Company, Marietta, Georgia

A highly efficient computer analysis has been developed for predicting transonic nacelle/inlet flowfields. This algorithm can compute the three-dimensional transonic flowfield about axisymmetric or asymmetric nacelle/inlet configurations at zero or nonzero incidence. The flowfield is determined by solving the full-potential equation in conservative form on a body-fitted curvilinear computational mesh. The difference equations are solved using the AF2 approximate factorization scheme. The effects of boundary-layer viscous entrainment are approximated in the inviscid algorithm by applying a surface transpiration velocity determined from the calculated boundary-layer growth. Computed results and correlations with existing methods and experiment are presented to illustrate application of the analysis.

Introduction

ACCURATE isolated nacelle/inlet flowfield predictions are required for nacelle contour optimization for both axisymmetric and asymmetric configurations. The prediction methods must be capable of analyzing three-dimensional transonic flowfields with the inclusion of embedded shock waves. Moreover, the prediction of the boundary-layer behavior and the viscous-inviscid interaction is required to verify that flow separation is not present under the anticipated operating conditions. The computational analyses which are developed must not only be accurate, but also efficient enough to be used repeatedly in parametric design studies. Techniques that divide the flowfield into an irrotational inviscid flow (potential flow) and an attached thin shear layer are applicable to nacelle/inlet assemblies at low to moderate incidence.

Efforts at computing three-dimensional transonic potential flows for nacelle/inlet geometries have been made by Chen and Caughey[1] and Reyhner.[2] Chen and Caughey[1] developed an algorithm for solving the full-potential equation on a body-fitted curvilinear grid for axisymmetric nacelles at incidence. An analytical grid mapping procedure was employed along with successive line over relaxation (SLOR) for solution of the difference equations. Reyhner[2] developed a three-dimensional nonconservative full-potential solution algorithm for axisymmetric or asymmetric nacelles. In this algorithm, a cylindrical mesh was used rather than a body-fitted curvilinear mesh. This eliminates any grid mapping problems, but may introduce difficulties in ensuring accurate boundary condition implementation at the nacelle surface since the mesh coordinate lines do not coincide with the body contour. SLOR was used for solution of the difference equations in the Reyhner algorithm. Brown[3] improved the accuracy and efficiency of this analysis by incorporating a local mesh refinement scheme used in conjunction with multigrid convergence acceleration.

The objective of this investigation[4] was to develop an accurate and highly efficient method for calculating the three-dimensional transonic flowfield about axisymmetric or asymmetric nacelle/inlet configurations at zero or nonzero incidence. The solution is obtained by solving the full-potential equation in conservation law form on a three-dimensional body-fitted curvilinear mesh which is numerically generated. The use of the conservative form of the equation ensures that mass continuity is satisfied when capturing embedded shock waves. The difference equations are solved using the AF2 approximate factorization algorithm.[5] The AF2 algorithm has been applied to the computation of two-dimensional transonic airfoil flows by Holst[6] and the computation of three-dimensional transonic wing flows by Holst and Thomas.[7] Increases in convergence speed by factors of 4 to 7 have been realized using the AF2 scheme instead of using the standard transonic relaxation scheme, successive line overrelaxation.

To approximately account for boundary-layer displacement effects, the nacelle inviscid solution algorithm has been linked to an integral axisymmetric boundary-layer analysis which is applied in a stripwise sense. A viscous correction to the inviscid solution is implemented by calculating an effective surface transpiration velocity from the computed boundary-layer growth which is then applied as a boundary condition at the body surface in the inviscid analysis.

The development of the isolated nacelle transonic flow algorithm represents a step toward the development of a combined wing/pylon/nacelle flow analysis program. The approach being taken in developing the multicomponent algorithm is to use a component-adaptive grid embedding scheme in which the global computational grid is composed of a series of overlapped component grids, where each component grid is optimized for a particular geometry such as the wing or nacelle. The AF2 algorithm is used to determine the full-potential equation solution on each grid with trivariate interpolation being used to transfer property information between the component grids. Preliminary results employing this scheme have been reported by Atta and Vadyak.[8]

Grid Topology and Generation

The flow solution is determined on a three-dimensional body-fitted curvilinear mesh. The computational mesh is obtained using two-dimensional numerical grid generation techniques for a series of meridional planes splayed circumferentially around the body (a meridional plane is a plane containing the longitudinal axis of the inlet).

Figure 1 illustrates the nacelle/inlet grid topology for a semi-infinite nacelle extended in the downstream direction. The base Cartesian coordinates are denoted by x, y, and z. Figure 1a shows the meridional plane grid topology, whereas

Received June 25, 1983; presented as Paper 83-1417 at the 19th Joint Propulsion Conference, Seattle, Wash., June 27-29, 1983; revision received June 1, 1984.

*Scientist, Advanced Flight Sciences Department. Member AIAA.

Fig. 1b illustrates the grid as viewed along the longitudinal axis of the inlet which is the x axis. The computational curvilinear coordinates are denoted by ξ, η, and ζ. The ξ coordinate is in the wraparound direction, initiates at the external outflow surface, and terminates at the compressor face outflow surface. The η coordinate is in the circumferential direction, initiates at the $\theta=0$ meridional plane, and terminates at the $\theta=2\pi$ meridional plane. The ζ coordinate is in the radial direction, initiates at the outer computational boundary (or centerline boundary), and terminates at the body surface. The $\theta=0$ and 2π meridional planes are coincident for isolated nacelle configurations. If a pylon were present, then the pylon geometry would be contained between these two meridional stations. The x-y coordinate plane is the symmetry plane for angle-of-attack cases.

The surface grid points are clustered in the region of the nacelle highlight (leading-edge point of the nacelle). The clustering is achieved by using a geometric stretching function which is expressed in terms of the arc length measured along the body from the highlight point. After the surface and outer boundary mesh point distributions have been determined, the interior mesh point locations are computed using the NASA Ames GRAPE[9] algorithm. The GRAPE program determines the interior field point coordinates by iteratively solving two coupled Poisson equations. For axisymmetric geometries, this two-dimensional grid generation procedure is applied for only one meridional plane, and the grid point locations on the remaining meridional planes are found using simple reflection techniques. For asymmetric geometries, the two-dimensional grid generation algorithm is applied for each meridional plane.

Figure 2 illustrates the rectangular computational domain that corresponds to the physical domain shown in Fig. 1. The physical space boundaries transform into boundaries in computational space. This allows for accurate and straightforward boundary condition implementation. The mesh points are equally spaced in computational space.

Figure 3 illustrates a typical meridional plane grid. The inlet centerline (x axis) represents a singularity in the three-dimensional grid mapping. The computational grid boundary is displaced a small distrance away from the x axis. An extrapolation and averaging technique, described later, is used to obtain flow properties on the centerline. It is advantageous to adjust the normal spacing near the external outflow surface to make a uniform radial point distribution along that surface. This produces a more favorable cell aspect ratio in this region, and thereby enhances stability and convergence in the flow solution algorithm.

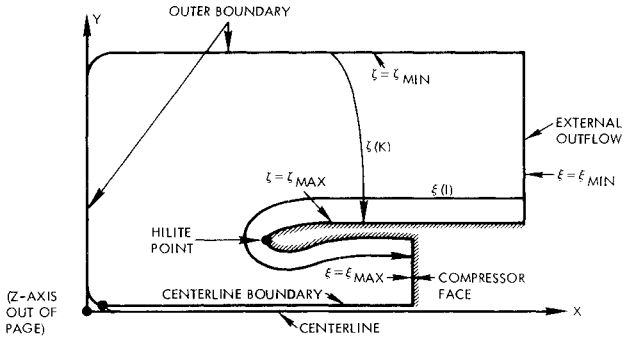

a) Meridional plane grid topology.

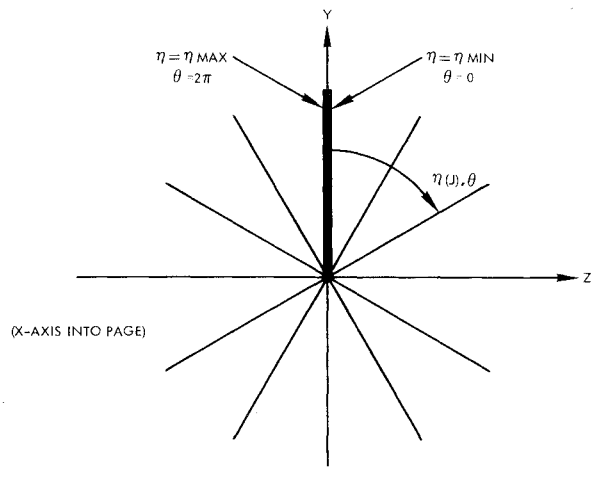

b) Grid viewed along x axis.

Fig. 1 Grid topology.

Governing Equations for the Inviscid Flow

The inviscid flow gas dynamic model is based on the assumption of steady potential flow which requires that the flow be both irrotational and isentropic. The governing equations for steady three-dimensional potential flow are given by

$$\left(\frac{\rho U}{J}\right)_\xi + \left(\frac{\rho V}{J}\right)_\eta + \left(\frac{\rho W}{J}\right)_\zeta = 0 \tag{1}$$

$$\rho = \left[1 - \frac{\gamma-1}{\gamma+1}\left(U\phi_\xi + V\phi_\eta + W\phi_\zeta\right)\right]^{1/(\gamma-1)} \tag{2}$$

where ξ, η, and ζ denote the system of curvilinear coordinates; U, V, and W are the contravariant velocity components in the ξ, η, and ζ directions, respectively; ρ the density; J the Jacobian of transformation from the Cartesian coordinate system (x,y,z) to the general curvilinear coordinate system (ξ,η,ζ); ϕ the velocity potential function; and γ the specific heat ratio. The density and contravariant velocity components are normalized by the stagnation density and critical sonic speed, respectively.

Equation (1) is the full-potential equation in strong conservation law form. It expresses mass continuity for steady three-dimensional flows. Equation (2) expresses entropy

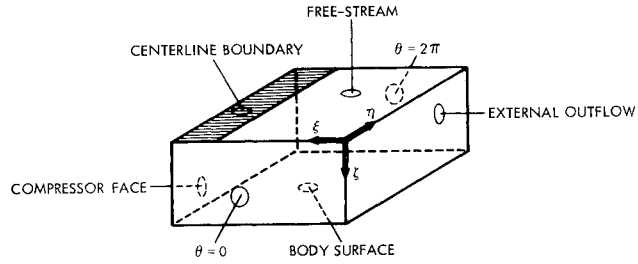

Fig. 2 Computational domain.

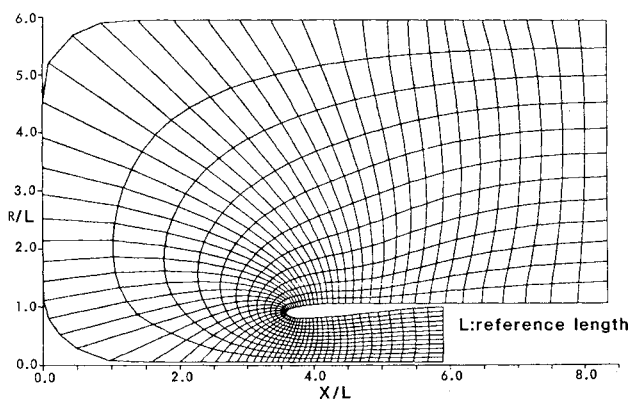

Fig. 3 Meridional plane grid.

conservation and is used to compute the density given the velocity potential field.

The contravariant velocity components can be expressed in terms of the Cartesian velocity components as

$$U = u\xi_x + v\xi_y + w\xi_z \tag{3}$$

$$V = u\eta_x + v\eta_y + w\eta_z \tag{4}$$

$$W = u\zeta_x + v\zeta_y + w\zeta_z \tag{5}$$

where u, v, and w denote the nondimensional velocity components along the x, y, and z Cartesian coordinate axes, respectively. The contravariant velocity components can be also expressed in terms of the velocity potential ϕ as

$$U = A_1\phi_\xi + A_4\phi_\eta + A_5\phi_\zeta \tag{6}$$

$$V = A_4\phi_\xi + A_2\phi_\eta + A_6\phi_\zeta \tag{7}$$

$$W = A_5\phi_\xi + A_6\phi_\eta + A_3\phi_\zeta \tag{8}$$

The metric parameters A_i and the Jacobian of transformation J are given by

$$A_1 = \xi_x^2 + \xi_y^2 + \xi_z^2 \qquad A_4 = \xi_x\eta_x + \xi_y\eta_y + \xi_z\eta_z$$

$$A_2 = \eta_x^2 + \eta_y^2 + \eta_z^2 \qquad A_5 = \xi_x\zeta_x + \xi_y\zeta_y + \xi_z\zeta_z$$

$$A_3 = \zeta_x^2 + \zeta_y^2 + \zeta_z^2 \qquad A_6 = \eta_x\zeta_x + \eta_y\zeta_y + \eta_z\zeta_z \tag{9}$$

$$J = \xi_x\eta_y\zeta_z + \xi_y\eta_z\zeta_x + \xi_z\eta_x\zeta_y - \xi_z\eta_y\zeta_x - \xi_y\eta_x\zeta_z - \xi_x\eta_z\zeta_y \tag{10}$$

The metric parameters are obtained numerically using standard second-order finite difference formulas to compute derivatives of the form x_ξ, x_η, x_ζ, y_ξ, etc. Then using metric relations, the inverse quantities ξ_x, η_x, etc., are determined. Substitution of these values into Eqs. (9) and (10) yields the A_i and Jacobian J.

Numerical Algorithm

The present numerical algorithm is based on the finite difference formulation used by Holst and Thomas[7] in computing transonic wing flows. In this algorithm, the full-potential equation residual is given by

$$L\phi_{i,j,k} = \vec{\delta}_\xi\left(\frac{\tilde{\rho}U}{J}\right)_{i+\frac{1}{2},j,k} + \vec{\delta}_\eta\left(\frac{\bar{\rho}V}{J}\right)_{i,j+\frac{1}{2},k} + \vec{\delta}_\zeta\left(\frac{\hat{\rho}W}{J}\right)_{i,j,k+\frac{1}{2}} \tag{11}$$

where $L\phi_{i,j,k}$ denotes the residual operator, and i, j, and k grid point indices in the ξ (wraparound), η (circumferential), and ζ (radial) directions, respectively. The magnitude of the residual $L\phi_{i,j,k}$ approaches zero as convergence is attained. The operators $\vec{\delta}_\xi(\ )$, $\vec{\delta}_\eta(\ )$, and $\vec{\delta}_\zeta(\ )$ are first-order-accurate backward finite difference operators (applied at midpoints) for the ξ, η, and ζ directions, respectively. The terms $\tilde{\rho}$, $\bar{\rho}$, and $\hat{\rho}$ are upwind-biased density coefficients given by expressions of the form

$$\tilde{\rho}_{i+\frac{1}{2},j,k} = [(1-\nu)\rho]_{i+\frac{1}{2},j,k} + \nu_{i+\frac{1}{2},j,k}\rho_{i+\frac{1}{2}+r,j,k} \tag{12}$$

where r denotes an upwind point along the ξ direction, and ν an artificial viscosity coefficient. In Eq. (12), the physical density ρ is computed using Eq. (2) with central differences used to determine the derivatives of ϕ. The artificial viscosity coefficient ν is given by

$$\nu = 0 \qquad M_{i,j,k} < 1$$

$$\nu = C(M_{i,j,k}^2 - 1) \qquad M_{i,j,k} > 1 \tag{13}$$

where M is the local Mach number, and C a user-specified constant. The artificial viscosity coefficient C typically ranges from 1.0 to 2.0 with the larger values producing greater upwinding. Expressions similar to Eq. (12) hold for $\bar{\rho}$ and $\hat{\rho}$ which effect upwinding in the η and ζ directions, respectively.

The finite difference equations are solved using the AF2 approximate factorization scheme which has proved to be significantly more efficient than SLOR schemes.[7] The AF2 algorithm is written in a three-step form as:

1) $$\left(\alpha - \frac{1}{A_k}\vec{\delta}_\eta A_j \overleftarrow{\delta}_\eta\right) g_{i,j}^n = \alpha\omega L\phi_{i,j,k}^n + A_{k+1} f_{i,j,k+1}^n \tag{14}$$

2) $$\left(A_k \mp \beta_\xi \vec{\vec{\delta}}_\xi - \frac{1}{\alpha}\vec{\delta}_\xi A_j \overleftarrow{\delta}_\xi\right) f_{i,j,k}^n = g_{i,j}^n \tag{15}$$

3) $$(\alpha + \overleftarrow{\delta}_\zeta) C_{i,j,k}^n = f_{i,j,k}^n \tag{16}$$

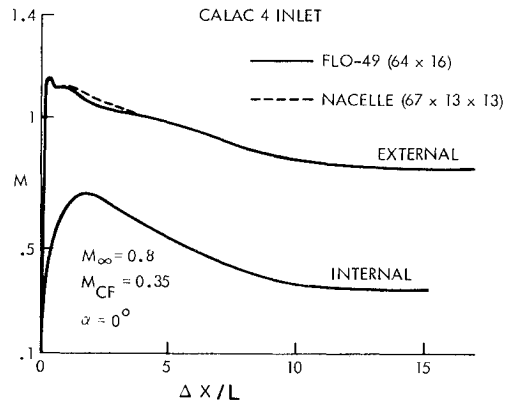

Fig. 4 Surface Mach number distribution for CALAC4 inlet at $M_\infty = 0.8$ and $\alpha = 0$ deg.

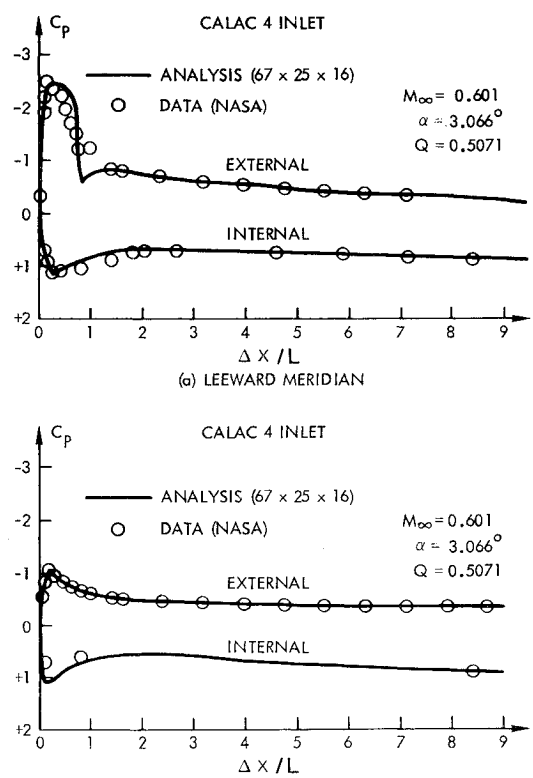

Fig. 5 Comparison of computed results with data for CALAC4 inlet at $M_\infty = 0.601$ and $\alpha = 3.066$ deg.

In Eqs. (14-16), α is a factorization parameter chosen to maintain stability and attain fast convergence, β_ξ a factor that controls the amount of dissipation required in regions of supersonic flow, ω a relaxation factor, n the interation number, $L\phi_{i,j,k}$ the mass residual [defined by Eq. (11)], f and g intermediate functions obtained during the solution process, and $C_{i,j,k}$ the potential function correction given by

$$C^n_{i,j,k} = \phi^{n+1}_{i,j,k} - \phi^n_{i,j,k} \tag{17}$$

The terms A_i, A_j, and A_k are defined by

$$A_i = (\tilde{\rho} A_1 / J)^n_{i-1/2,j,k} \tag{18}$$

$$A_j = (\tilde{\rho} A_2 / J)^n_{i,j-1/2,k} \tag{19}$$

$$A_k = (\tilde{\rho} A_3 / J)^n_{i,j,k-1/2} \tag{20}$$

In steps 1 and 2 (above) the g and f functions are obtained by solving a tridiagonal system of equations while, in step 3, the correction $C_{i,j,k}$ is obtained by solving a bidiagonal system of equations.

Boundary Conditions

The density and potential function on the outer boundary are held at their freestream values during the iterative solution procedure. The grid centerline boundary is offset a small distance from the centerline (x axis) to avoid the mapping singularity. To determine property values on the centerline, an extrapolation and averaging procedure is employed. For each meridional plane, the potential function values at interior mesh points are used to extrapolate for the potential values on the centerline. A circumferential averaging of the extrapolated values is then performed for each wraparound station. The potential values for points on each meridional plane centerline boundary are then updated by interpolation using property information from the centerline and interior field points. This updating is performed for every iteration. The property values on the outer and centerline boundaries are then used as Dirichlet boundary conditions for the ensuing iteration.

At the body surface, the contravariant velocity W_s in the ζ-coordinate direction is specified. The velocity W_s is zero for an inviscid calculation as this satisfies the flow tangency condition. To account for boundary-layer displacement effects, an effective W_s is calculated from the computed boundary-layer growth and then applied as a surface transpiration velocity boundary condition. The calculation of W_s for the viscous correction case is described later. Once W_s is specified, the term ϕ_ζ is calculated from

$$\phi_\zeta = (W_s - A_5\phi_\xi - A_6\phi_\eta)/A_3 \tag{21}$$

where the derivatives ϕ_ξ and ϕ_η are found using second-order differencing in the ζ = const boundary surface.

At the compressor face and external outflow surfaces, the contravariant velocity U_0 in the ξ coordinate direction is specified. Given the local Cartesian velocity components u, v, and w, and the metric quantities ξ_x, ξ_y, and ξ_z, U_0 can be determined using Eq. (3). At the compressor face, the flow is assumed to be uniform and in the axial (x) direction. The local flow velocity and density are fixed by specification of the required engine mass flow rate. At the external outflow surface, it is assumed that the freestream velocity components are recaptured. Once U_0 has been determined, the term ϕ_ξ is calculated from

$$\phi_\xi = (U_0 - A_4\phi_\eta - A_5\phi_\zeta)/A_1 \tag{22}$$

where the derivatives ϕ_η and ϕ_ζ are found using second-order differencing in the ξ = const boundary surface.

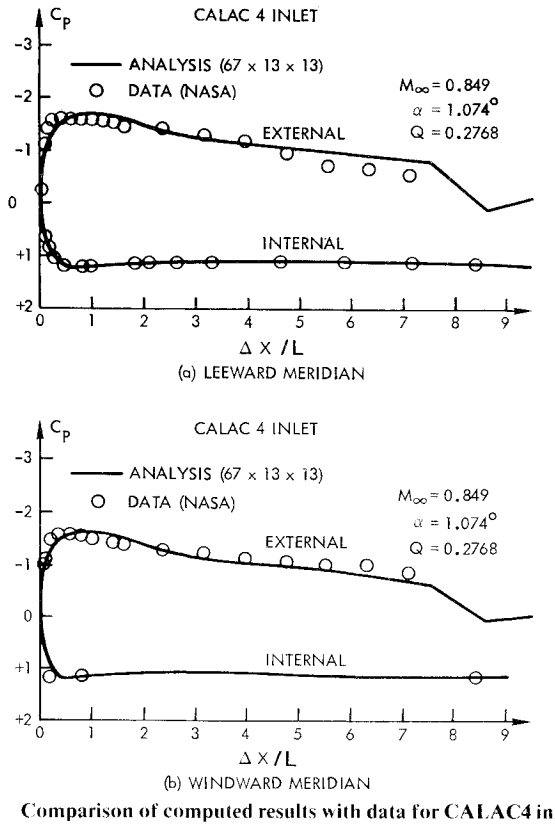

Fig. 6 Comparison of computed results with data for CALAC4 inlet at $M_\infty = 0.849$ and $\alpha = 1.074$ deg.

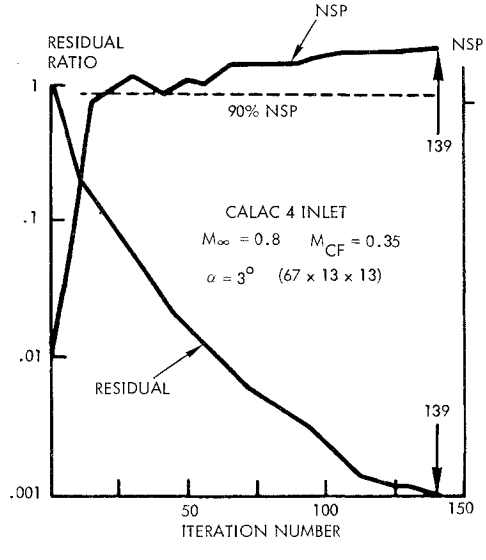

Fig. 7 Number of supersonic points (NSP) and error vs iteration number.

At the mesh corner points ($\xi = \xi_{min}$; $\zeta = \zeta_{max}$) and ($\xi = \xi_{max}$; $\zeta = \zeta_{max}$), two boundary conditions are enforced since both U and W are fixed. In these cases, ϕ_η is computed using second-order differencing, and the derivative ϕ_ζ is found from

$$\phi_\zeta = [A_5(U_0 - A_4\phi_\eta) - A_1(W_s - A_6\phi_\eta)]/(A_5^2 - A_1A_3) \tag{23}$$

The term ϕ_ξ is then calculated using Eq. (22).

In calculating the residual values for points on the body and outflow surfaces, the surface contravariant velocity along the direction normal to the surface is used directly.

Boundary conditions are also required for the intermediate functions f and g. For isolated nacelle geometries, periodic

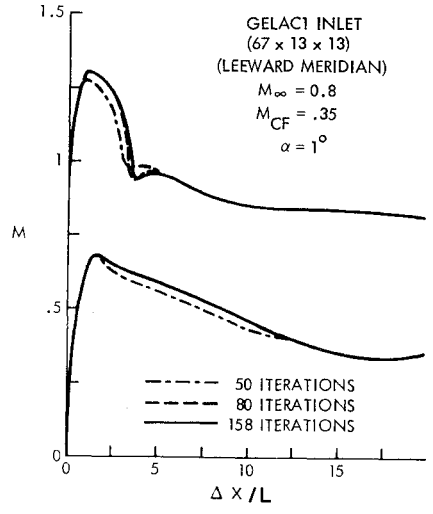

Fig. 8 Evolution of surface solution with iteration number.

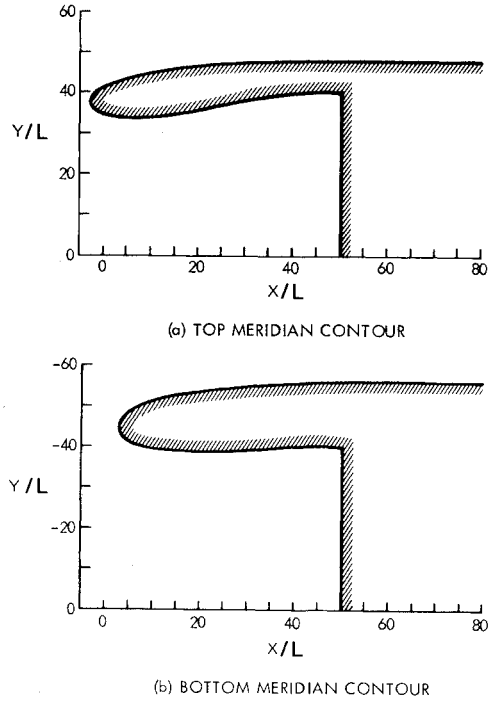

Fig. 9 Asymmetric nacelle/inlet meridian contours.

boundary conditions are used in the η-coordinate direction. In the ξ-coordinate direction, the condition $f_\xi = 0$ is imposed at both the compressor face and external outflow surfaces.

Initialization

Significant improvements in convergence speed have been realized by initializing the potential function field using different procedures for the external and internal flows. The potential field initialization for the external flow is performed using freestream velocity components. For the internal flow initialization, the local velocity is assumed to be axial and is computed using a Mach number determined from the implicit relation

$$M\left(1+\frac{\gamma-1}{2}M^2\right)^{\frac{-(\gamma+1)}{2(\gamma-1)}} = \left(\frac{A_{cf}}{A}\right)M_{cf}\left(1+\frac{\gamma-1}{2}M_{cf}^2\right)^{\frac{-(\gamma+1)}{2(\gamma-1)}} \tag{24}$$

where M and M_{cf} denote the local and compressor face Mach numbers, respectively, and A and A_{cf} the local and compressor face flow areas, respectively. Equation (24) was obtained using one-dimensional gasdynamic formulas which express mass continuity for the captured stream tube. To determine the internal potential field, a trapezoidal-rule integration is used.

Numerical Stability

During the course of program development, it was found necessary to impose a potential correction underrelaxation in the iterative process when calculating the solution at points near the centerline. The centerline represents a singularity in the three-dimensional grid mapping. Without the underrelaxation, somewhat large potential function corrections would occur at mesh points near the centerline.

A von Neumann linear stability analysis was conducted for the three-dimensional AF2 algorithm using the conservative form of the full-potential equation expressed in curvilinear coordinates. Simplified and linearized forms of the correction and residual opertors were obtained by assuming that flow was subsonic ($\rho \approx 1$), that there was a slow spatial variation of the metrics ($A_{i\xi} = 0$, etc.), and that the grid was approximately orthogonal. Expressions were derived for the amplification factor in terms of A_1, A_2, A_3, J, ω, and α. The analysis indicated unconditional linear stability if $0<\omega<2$ and $\alpha>0$. When numerical values for the metric terms were substituted into the amplification factor expressions, low amplification factor values were obtained for the external and internal flow mesh points near the body surface. Higher amplification factor values were obtained near the centerline. Fastest convergence is attained if the amplification factor magnitude is near zero.

To compensate for this effect, a simple potential function correction underrelaxation scheme was incorporated for mesh points close to the centerline. The potential function updating is thereby performed using

$$\phi^{n+1}_{i,j,k} = \phi^{n}_{i,j,k} + \sigma C^{n}_{i,j,k} \tag{25}$$

where $\sigma < 1.0$ at mesh points close to the centerline and $\sigma = 1.0$ elsewhere (standard algorithm).

Viscous Correction Calculation

To approximately account for viscous correction effects, the nacelle/inlet inviscid flow algorithm has been linked to the Sasman-Cresci axisymmetric integral boundary-layer program[10] in a stripwise or meridional plane sense. Instead of using a computed displacement thickness added on to the original nacelle contour to account for boundary-layer effects, this algorithm computes an effective surface transpiration velocity determined from the calculated boundary-layer growth. This transpiration velocity is then applied as a surface boundary condition in the full-potential algorithm. Because an integral boundary-layer analysis is used, this method yields an efficient means of effecting a viscous correction which is approximate due to the neglect of boundary-layer cross-flow influences. This method also has a distinct advantage in that the computational grid for the potential-flow solver does not have to be regenerated after the correction is made as would be the case if a displacement thickness approach were employed. The viscous correction calculation is part of the overall algorithm and is performed periodically as the inviscid iteration procedure progresses.

To determine the effective contravariant transpiration velocity W_ζ to be applied at the body surface in Eq. (21), a strip boundary-layer calculation is made using the current potential flow surface solution for a given meridional plane. With the computed boundary-layer displacement thickness δ^* distribution, the physical transpiration velocity $\tilde{V}_t$ is found

from

$$\tilde{V}_I = \frac{I}{\tilde{\rho}_e} \frac{\partial}{\partial \tilde{s}} (\tilde{\rho}_e \tilde{u}_e \tilde{\delta}^*) \tag{26}$$

where $\tilde{\rho}_e$ and $\tilde{u}_e$ denote the dimensional density and streamwise velocity at the boundary-layer edge, respectively, and $\tilde{s}$ denotes the arc length measured from the current meridional plane stagnation point. The velocity $\tilde{V}_I$ is orthogonal to the nacelle surface. This velocity is normalized by the critical sonic speed and is then resolved into Cartesian velocity components. At this stage, the contravariant velocity W_ζ is computed from Eq. (5) using the surface metrics. The viscous correction transpiration velocity updating is typically performed every 10 ~ 20 iterations. Smoothing and underrelaxation procedures have been incorporated to aid stability when the viscous correction is applied for strong shock cases.

Numerical Results

Selected numerical results are now presented to illustrate application of the analysis. Both axisymmetric and asymmetric nacelle/inlet configurations operating at zero and nonzero incidence are considered.

The first set of computed results are for a recently designed Lockheed axisymmetric nacelle/inlet configuration called the CALAC4 inlet. Figure 4 illustrates the computed Mach number distributions (without viscous correction) for both the external and internal nacelle surfaces. The results shown are for a freestream Mach number M_∞ of 0.8, an effective compressor face Mach number M_{cf} of 0.35, and an incidence α of 0 deg. Plotted is the surface Mach number M vs the nondimensional distance ($\Delta X/L$) from the nacelle highlight. Since the geometry is axisymmetric and the angle of attack is zero, the flowfield will be axisymmetric. Also shown in Fig. 4 are the results of the Jameson FLO-49 axisymmetric flow nacelle code.[11] The Jameson code is a two-dimensional full-potential finite volume nacelle algorithm which uses SLOR with multigrid convergence acceleration. It is limited to predicting the flow for axisymmetric nacelles at zero incidence. Referring to Fig. 4, it can be seen that the two analyses agree very well. The Jameson program computation employed a grid with 64 wraparound stations and 16 radial stations. The three-dimensional nacelle program computation employed a grid with 67 wraparound stations, 13 circumferential stations, and 13 radial stations.

Figures 5 and 6 show correlations between the analysis and experimental data[12] for the CALAC4 inlet. In Fig. 5, the computed surface pressure coefficient C_p and wind tunnel data are compared for a case with $M_\infty = 0.601$, $\alpha = 3.066$ deg, and an inlet capture ratio Q of 0.507. The capture ratio is defined as the ratio of freestream capture area to the inlet highlight area. Figure 5 illustrates the results for both the external and internal surfaces for both the leeward and windward meridians. The agreement between the results of the numerical analysis and experiment is very good. The numerical results illustrated in Fig. 5 were obtained using a computational grid with 67 wraparound stations, 25 circumferential stations, and 16 radial stations. The same case was executed using a $67 \times 13 \times 13$ grid. The resulting surface solutions for the two grids were almost identical except that the C_p peak on the windward meridian's external surface was predicted better using the finer grid.

Figure 6 illustrates the computed surface pressure coefficient distributions and experimental data for the CALAC4 inlet operating at the conditions of $M_\infty = 0.849$, $\alpha = 1.074$ deg, and $Q = 0.2768$. This represents a difficult test case because of the low capture ratio which requires that most of flow be spilled around the external cowling thereby generating a large region of supersonic flow. The Mach number corresponding to the peak negative pressure coefficient is approximately 2.1. Nonetheless, excellent agreement is obtained with the data using a $67 \times 13 \times 13$ grid. The low capture ratio case required increasing the artificial viscosity and time-like dissipation coefficients beyond their default values. This ensures numerical stability but decreases convergence speed.

Figures 7 and 8 illustrate the rapid convergence properties of the present approximate factorization algorithm. The variation of the number of supersonic points (NSP) with iteration number is plotted in Fig. 7 for the flowfield solution of the CALAC4 inlet operating at a freestream Mach number of 0.8, a compressor face Mach number of 0.35, and $\alpha = 3$ deg angle of attack. For this case, convergence, which corresponds to a three-order-of-magnitude reduction in maximum residual, was attained in 139 iterations. The value of NSP increases very quickly with iteration number. After approximately 25 iterations, the NSP level has already achieved 90% of its final value. Figure 7 also illustrates error reduction as a function of iteration number for this case. On the ordinate axis is plotted the log of the ratio of the absolute value of the maximum residual on the current iteration to that on the first iteration. (The results were plotted every 20 iterations.) After approximately 60 iterations, the maximum residual has been reduced by two orders of magnitude. Figure 8 presents the evolution of the surface solution with iteration number for the flowfield computation of another Lockheed axisymmetric inlet design called the GELAC1 inlet operating at $M_\infty = 0.8$, $M_{cf} = 0.35$, and $\alpha = 1$ deg. Shown in this figure are the computed solutions at 50, 80, and 158 iterations for the leeward meridian. The solution at 158 iterations represents the final converged solution at which point the maximum residual has been reduced by three orders of magnitude. After 50 iterations, a good approximation to the fully converged solution has been attained. The difference between the fully converged solution and that at 80 iterations is very minor. A characteristic of the AF2 algorithm is the rapid development of the surface Mach number and pressure distributions.

Flow computations have also been performed for an asymmetric nacelle/inlet configuration. The configuration under study is a recent Lockheed drooped-inlet design in which the inlet contour has circumferential variation both in section shape and in length from the highlight point to the compressor face. The front of the inlet is tilted downward with respect to the engine centerline for the purpose of aligning the inlet with the local flow direction underneath the wing. This reduces cruise drag while maintaining the engine thrust vector in the proper orientation. Figure 9 illustrates the nacelle/inlet contours for the top ($\theta = 0$) and bottom ($\theta = 180$ deg) circumferential stations. The nacelle has one plane of geometric symmetry, and thereby the computational grid is generated for one-half of the computational domain and then reflected about the symmetry axis to obtain the other half.

For an asymmetric nacelle, the flow will be three-dimensional even at zero incidence. Computed surface Mach number contours for the top ($\theta = 0$) and bottom ($\theta = 180$ deg) meridians of the asymmetric nacelle are presented in Fig. 10. These results are for a freestream Mach number M_∞ of 0.8, a compressor face Mach number M_{cf} of 0.35, and zero incidence ($\alpha = 0$). Asymmetry exists in the computed solution with the lower external surface producing a higher local Mach number than the top meridian at this angle of attack.

The effect of viscous correction using the surface transpiration velocity method on the computed surface pressure distribution for the GELAC1 axisymmetric nacelle/inlet configuration is shown in Fig. 11. The results given are for a freestream Mach number of 0.8, a compressor face Mach number of 0.35, zero incidence, and a Reynolds number of 2×10^6/ft. The results are for the external nacelle surface region slightly downstream of the highlight point in the region of peak surface Mach number. The effect of viscous correction is to slightly displace the pressure distribution curve forward in the region of rapid flow compression, and to slightly smear the shock pressure distribution.

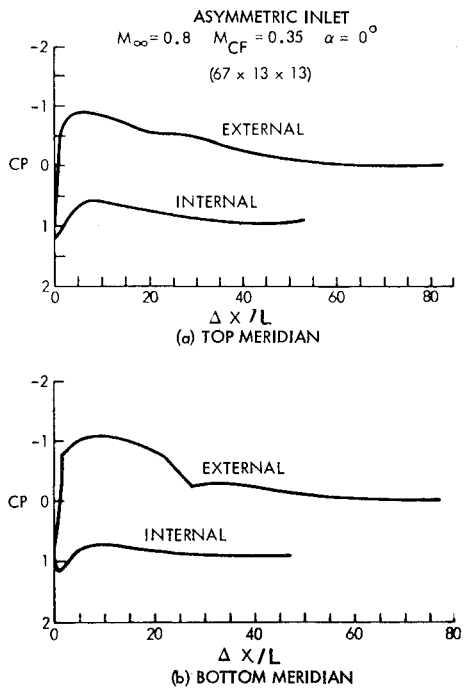

Fig. 10 Surface pressure distribution for asymmetric inlet at $M_\infty = 0.8$ and $\alpha = 0$ deg.

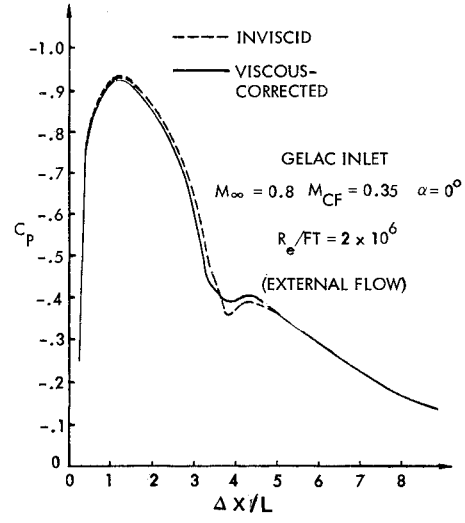

Fig. 11 Comparison of inviscid and viscous-corrected pressure distributions.

Computer Execution Time

Typical computation times for three-dimensional flow solutions using the nacelle/inlet algorithm are 15-25 min for subcritical cases and 35-50 min for supercritical cases on a DEC VAX-11/780 computer using a $67 \times 13 \times 13$ computational grid. The algorithm has also been executed on the NASA Ames CRAY-1 Class VI vector processor. Typical computation times for three-dimensional supercritical flow solutions using the CRAY-1 are on the order of 90 s of CPU time. No special effort has yet been made in vectorizing the program for use on the CRAY-1. Consequently, substantial improvements in the required execution time can be realized by restructuring the scalar code to benefit more fully from the CRAY vector processing capabilities. It is estimated that by doing this the execution time could be reduced by a factor of 5-6.

Conclusions

A highly efficient and accurate algorithm has been developed for computing transonic three-dimensional nacelle/inlet flowfields. The flowfield is determined by solving the full-potential equation in conservative form on a body-fitted curvilinear grid using the AF2 approximate factorization scheme. A viscous correction has been implemented by linking the inviscid flow algorithm with an integral boundary-layer analysis that is applied in a stripwise sense. The results of the present analysis agree well with those produced by existing methods when axisymmetric flowfields are computed, and agree well with experimental data for three-dimensional flowfields. The reliability, ease of use, and fast convergence properties of the present algorithm make it suitable for use in the design environment.

Acknowledgment

This effort was sponsored in part by the NASA Ames Research Center under Contract NAS2-11285 and in part by the Lockheed Independent Research and Development Program.

References

[1] Chen, L. T. and Caughey, D. A., "A Higher-Order, Finite-Difference Scheme for Transonic Flowfields Around Complex 3-D Geometries," AIAA Paper 79-1460, 1979.

[2] Reyhner, T. A., "Transonic Potential Flow Computation about Three-Dimensional Inlets, Ducts, and Bodies" *AIAA Journal*, Vol. 19, Sept. 1981, pp. 1112-1121.

[3] Brown, J. J., "A Multigrid Mesh-Embedding Technique for Three-Dimensional Transonic Potential Flow Analysis," AIAA Paper 82-0107, Jan. 1982.

[4] Vadyak, J. and Atta, E. H., "A Computer Program for the Calculation of Three-Dimensional Transonic Nacelle/Inlet Flowfields," NASA CR-166528, 1983.

[5] Ballhaus, W. F., Jameson, A., and Albert, J., "Implicit Approximate-Factorization Schemes for Steady Transonic Flow Problems," *AIAA Journal*, Vol. 16, June 1978, pp. 573-579.

[6] Holst, T. L., "An Implicit Algorithm for the Conservative Transonic Full Potential Equation Using an Arbitrary Mesh," *AIAA Journal*, Vol. 17, Oct. 1979, pp. 1038-1045.

[7] Holst, T. L. and Thomas, S. D., "Numerical Solution of Transonic Wing Flow Fields," AIAA Paper 82-0105, Jan. 1982.

[8] Atta, E. H. and Vadyak, J., "A Grid Interfacing Zonal Algorithm for Three-Dimensional Transonic Flows about Aircraft Configurations," AIAA Paper 82-1017, June 1982.

[9] Sorensen, R. L., "A Computer Program to Generate Two-Dimensional Grids About Airfoils and Other Shapes by Use of Poisson's Equation," NASA TM-81198, 1980.

[10] Sasman, P. K. and Cresci, R. J., "Compressible Turbulent Boundary Layer with Pressure Gradient and Heat Transfer," *AIAA Journal*, Vol. 4, Jan. 1966.

[11] Jameson, A., "Transonic Flow Analysis for Axially Symmetric Inlets with Centerbodies," Antony Jameson and Associates, Inc., Princeton, N.J., Rept. 2, 1981.

[12] Results from the Joint NASA/Industry Subsonic Inlet Design Technology Testing Program conducted at NASA Langley, 1982.